Giant, 12, 2022, 100121

Full-length article

One-step Method to Fabricate Poly(ethylene terephthalate)/$Gd(OH)_3$ Magnetic Nanofibers Towards MRI-active Materials with High T_1 Relaxivity and Long-term Visibility

Yifan Jia [a], Weiwen Yuan [b], Mengmeng Xu [a], Congyi Yang [a], Lei Chen [a], Shuo Wang [a], Paul D. Topham [c], Guoxuan Luo [b], Mo Wang [b], Yong Zhang [b,*], Guihua Jiang [b,*], Qianqian Yu [a,*], LinGe Wang [a,*]

[a] South China Advanced Institute for Soft Matter Science and Technology, School of Emergent Soft Matter, Guangdong Provincial Key Laboratory of Functional and Intelligent Hybrid Materials and Devices, South China University of Technology, Guangzhou 510640, China
[b] Guangdong Second Provincial General Hospital, Guangzhou 510317, China
[c] Chemical Engineering and Applied Chemistry, School of Infrastructure and Sustainable Engineering, College of Engineering and Physical Sciences, Aston University, Birmingham, B4 7ET, UK

Keywords: Electrospinning, Magnetic nanofibers, Magnetic resonance imaging, Long-term visibility, Gadolinium, T_1 positive contrast

Magnetic resonance imaging (MRI)-active polymers exhibit unique advantages for *in vivo* diagnosis. Here, in order to endow electrospun fibers with long-term T_1 positive MRI visibility, MRI contrast agent (CA), $Gd(OH)_3$, is introduced in a new, extremely convenient method. Crucially, $GdCl_3$ is reacted with NaOH *in situ* during electrospinning, with flexibility to deliver both well-dispersed and aggregated $Gd(OH)_3$ clusters within a poly(ethylene terephthalate) (PET) matrix. T_1 and T_2 relaxivities of $Gd(OH)_3$ in PET nanofibers are studied. Well-dispersed $Gd(OH)_3$ (sub-nanometer in size) exhibits 34 times higher T_1 relaxivity than aggregated nanoparticles when embedded within the fibers. The morphology, structure, magnetic properties, tensile properties, imaging performance and biosafety of the PET/$Gd(OH)_3$ composite fibers are evaluated to identify the optimum conditions to produce new materials with balanced properties, excellent *in vivo* positive contrast and approximately 139 days imaging lifetime. Comparing this sample with a commercial CA, only 0.32 wt.% Gd loading is needed to attain similar MRI signal intensity. In summary, PET/$Gd(OH)_3$ long-term MRI-active fibers show great potential for future biomedical applications and the study also provides a promising new general strategy to enhance the MRI T_1 positive contrast of electrospun fibers of a whole host of other systems.

* Corresponding authors.
E-mail addresses: zhangyongsey@163.com (Y. Zhang), jianggh@gd2h.org.cn (G. Jiang), yuqianqian@scut.edu.cn (Q. Yu), lingewang@scut.edu.cn (L. Wang).
Received 10 September 2022; Received in revised form 8 October 2022; Accepted 12 October 2022

https://doi.org/10.1016/j.giant.2022.100121

1 Introduction

Due to the versatility of electrospinning for processing many biopolymers, providing excellent control over the resultant fibrous structure and ability to encapsulate various organic and inorganic materials, electrospun fibers have been widely studied and applied in tissue engineering [1–11], drug delivery [12–15], cancer therapy [16–22], etc. Magnetic resonance imaging (MRI), as one of the most powerful soft tissue imaging techniques [23], has been an essential examination tool for clinical diagnosis. However, most polymers cannot provide enough MRI signal to be readily imaged (see Supporting Information Table S1). This inability to acquire *in vivo* information of polymeric fibers via MRI has obstructed the evaluation of postoperative effectiveness and further treatment [24]. Therefore, MRI-active materials including fiber [25–30], hydrogel [28], foam [31], stent [32] and coating [33–35] are desired and researched for enhancing their exploitation in biomedical applications.

The signal of MRI is provided by ^{1}H nuclei (e.g., of water inside the body). To visualize a polymer, magnetic MRI contrast agents (CAs) are incorporated to shorten the T_1 and T_2 relaxation times of water molecules adjacent to polymer [35,36]. Thus, those water molecules could provide higher signal intensity (observed brighter in images) under a T_1WI (T_1 weighted imaging) sequence and lower signal intensity (observed darker in images) under a T_2WI (T_2 weighted imaging) sequence [37], which respectively leads to positive and negative contrast of the polymer compared with the environment.

In order to long-term visualize electrospun polymeric fibers under MRI, several approaches have been demonstrated by blending or surface modifying water-insoluble magnetic nanoparticles, such as iron oxide nanoparticles (IONPs) [38,39] and ferritin clusters [40], into or onto electrospun fibers. However, to the best of our knowledge, this has been limited to negative contrast enhancement. The positive contrast of IONPs and ferritin [41–43] was lost when incorporated into polymer fibers. In practice, positive contrast is preferred for materials with nearly no MRI signal, since negative contrast can be confused with low signal areas (such as bone, vasculature adjacent tissue, tissue-air interfaces or image artifacts) [44,45]. To obtain positive contrast, gadolinium-based CAs, gadolinium-diethylenetriaminepentaacetate hydrate (Gd-DTPA) [46] and gadodiamide [47], were both loaded in electrospun fibers. However, due to their high water-solubility, CAs were rapidly dissolved in the environment. The *in vivo* half-lives of Gd-DTPA (13.1 minutes [48]) and gadodiamide (1.3 hours [49]) were too short for them to provide long-term MRI visibility. Thus, a water-insoluble CA with high T_1 relaxation acceleration efficiency (i.e., T_1 relaxivity) is needed to endow electrospun fibers with long-term positive contrast. The underlying mechanism of the loss of IONPs and ferritin's positive contrast within fibers also needs to be rigorously studied for enhancing T_1 relaxivity.

According to Solomon–Bloembergen–Morgan (SBM) theory, the CA T_1 relaxivity (r_1) is inversely proportional to the sixth power of the distance between the CA and coordinated water molecules [50,51]. The aggregation of nanoparticulate CAs dramatically influences $r_1$due to the coupling failure between water molecules and metals hidden inside the core of aggregates [52]. For example, the r_1 value of uniformly distributed ferritin (1290 L mmol^{-1} s^{-1}) was shown to be significantly higher than its aggregated counterpart (0.674 L mmol^{-1} s^{-1}) [41]. The same phenomenon was also reported for IONPs [53] in aqueous solution. Based on these findings, we surmise that the unexpected loss of positive contrast reported in previous studies could be attributed to CA aggregation within the fibers.

In the work herein, we introduce a new, one-step fabrication process of composite magnetic fibers with high T_1 relaxivity and long-term MRI visibility. We have developed a versatile method to disperse a CA at sub-nanometer length scales within a polymeric matrix to generate maximum surface area for enhancing the coupling between water molecules and CA. A representative FDA-approved bioinert polymer poly(ethylene terephthalate) (PET) [54], which has been used for fabricating artificial tendon [3], blood vessel [55], surgical suture [56] was selected to encapsulate positive CA $Gd(OH)_3$. $Gd(OH)_3$ was reported to be biocompatible, highly efficient (r_1 = 12.3 L mmol^{-1} s^{-1}) [57] and water-insoluble (k_{sp} = 8.2 × 10^{-23}) [58]. Therefore, it was an ideal candidate for this research. $GdCl_3$ was reacted with NaOH *in situ* during the electrospinning process to form $Gd(OH)_3$. We utilized the characteristics of electrospinning (highly viscous spinning solution, due to polymer chain entanglement and rapid volatilization of solvent) to reduce the mobility of ions and prevent the aggregation of Gd^{3+} during the fabrication process, as shown in Fig. 1a. Nanofibers were collected into NaOH/water which could further extract residual solvent from the fibers, suppress Gd^{3+} mobility, and reduce the probability of aggregation. PET nanofibers loaded with well-dispersed $Gd(OH)_3$ (sub-nanoscale) and aggregated $Gd(OH)_3$ nanoparticles (tens of nanometers in size) were both fabricated (see Table 1) to probe the underlying mechanism of contrast enhancement. Considering relaxivity, mechanical properties, biosafety and imaging ability, animal studies were performed on three composite nanofibers with extremely low $Gd(OH)_3$ content to evaluate their feasibility for further biomedical applications.

2 Experimental

2.1 Materials

PET (4210G, M_w = 2.5 × 10^4 g/mol, PDI = 2) was obtained from Huizhou South Asia Group Co., Ltd, China. Dichloromethane (DCM), trifluoroacetic acid (TFA), NaOH and $GdCl_3{\cdot}6H_2O$ were analytical pure and purchased from Aladdin (used without further purification). Omniscan (Gd-DTPA) was bought from General Electric Pharmaceutical (Shanghai) Co., Ltd. Epoxy resin embedding kit was bought from Electron Microscopy China. Cell counting kit-8 (CCK-8) was bought from Beyotime Institute of Biotechnology, China. 96-well plates were purchased from NEST Biotechnology, China.

2.2 Preparation of electrospun fibers

Fiber preparation has been published in the filed patent [59]. Briefly, PET was dissolved in DCM:TFA = 1:1 (wt.:wt.) [60] before various amounts of $GdCl_3{\cdot}6H_2O$ were added to form PET/$GdCl_3$ solutions with Gd^{3+}:PET = 0.1, 0.2, 0.3, 0.5, 1, 2, 3, and 5: 100 (wt.:wt.). After 24h stirring at room temperature, PET and PET/$GdCl_3$ solutions were loaded in a syringe with 0.72 mm

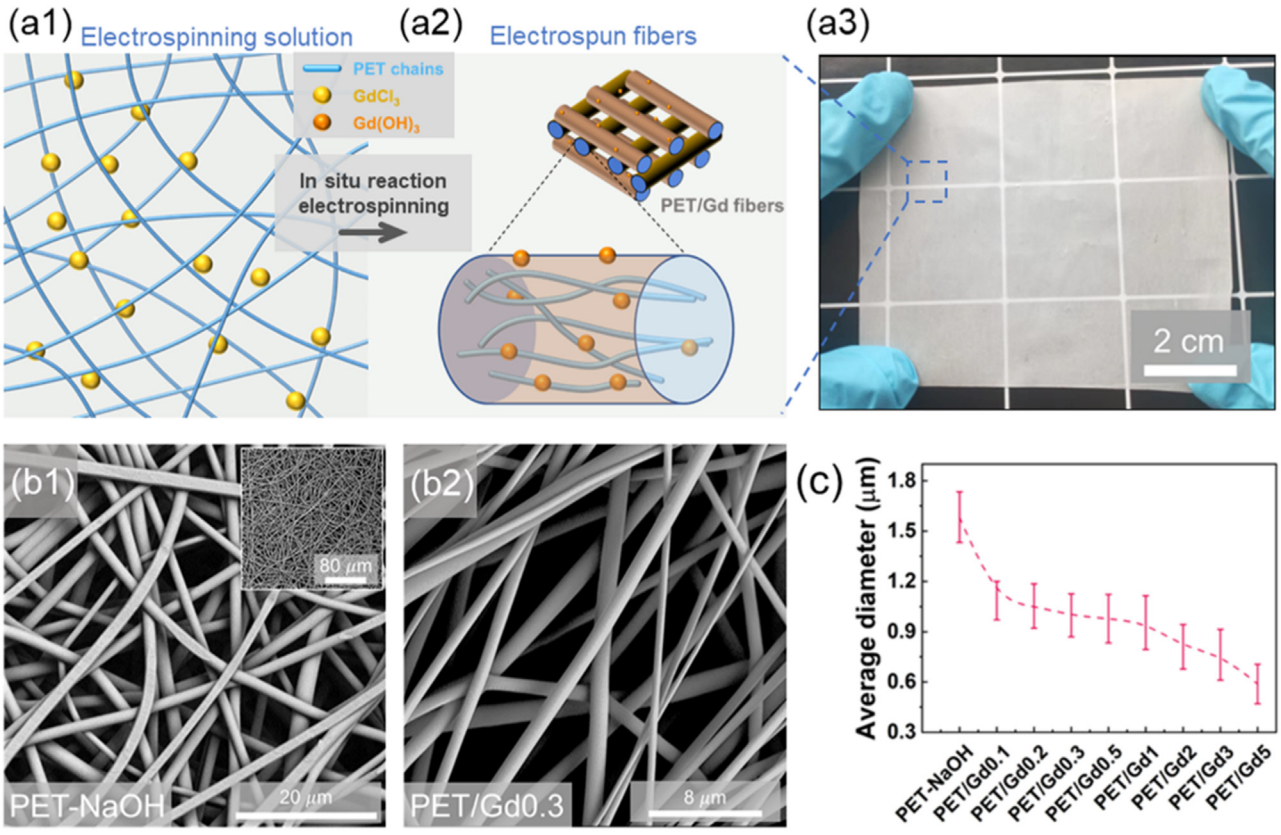

Fig. 1

Electrospun MRI-active fibers. Cartoon illustration of (a1) the separation of $GdCl_3$ due to the restriction of movement arising from the rapid removal of solvent and fixation within the dense mesh of polymer chains, following dissolution of $GdCl_3$ in the solution prior to deposition by electrospinning and (a2) $Gd(OH)_3$ loaded and well dispersed within electrospun PET fibers. (a3) Digital photograph of PET/Gd0.3 fibers. (b1-b2) SEM images of PET-NaOH and PET/Gd0.3 fibers. (c) Average fiber diameter values from more than 60 measurements from the SEM images.

Table 1

Nomenclature of fibers and their key features.

No.	Electrospun fibers	Gd^{3+} : PET (wt.)	Fiber collector	$Gd(OH)_3$ state[a]	Relaxivity
1	PET-NaOH	0:100	NaOH solution	/	/
2	PET	0:100	Aluminum plate	/	/
3	PET/Gd0.1	0.1:100	NaOH solution	Well dispersed	High
4	PET/Gd0.2	0.2:100	NaOH solution	Well dispersed	High
5	PET/Gd0.3	0.3:100	NaOH solution	Well dispersed	High
6	PET/Gd0.5	0.5:100	NaOH solution	Partially crystalline aggregates	High
7	PET/Gd1	1:100	NaOH solution	Partially crystalline aggregates	Low
8	PET/Gd2	2:100	NaOH solution	Partially crystalline aggregates	Low
9	PET/Gd3	3:100	NaOH solution	Partially crystalline aggregates	Low
10	PET/Gd5	5:100	NaOH solution	Partially crystalline aggregates	Low
11	PET/$GdCl_3$	5:100	Aluminum plate	/	/

[a] See $Gd(OH)_3$ distribution in Fig. 2 and Supporting Information Figure S6.

inner diameter steel needle. NaOH/water solution at pH = 10 was prepared as the collector. +17 kV and -1 kV voltage from high voltage supply (DW-P303-1ACF0, Dongwen high voltage power supply Co., Ltd., China) were applied to the needle and collector, respectively. The electrospinning solution was fed at 2 mL/h by syringe pump (LSP01-1A, Longer precision pump Co., Ltd., China). The distance between the needle and collector was maintained at 20 cm. The ambient temperature was 15 to 25 °C and relative humidity was 60% to 80%. After electrospinning, fibers were moved to a NaOH/water solution at pH = 10 for further 48 h reaction. Then washed to neutral pH and dried in the oven at 40 °C. According to Gd concentration, these fibers were named as PET-NaOH (no $GdCl_3 \cdot 6H_2O$ added, but collected by and reacted with NaOH solution), PET/Gd0.1, PET/Gd0.2, PET/Gd0.3, PET/Gd0.5, PET/Gd1, PET/Gd2, PET/Gd3 and PET/Gd5.

To compare the effect of NaOH/water collector, two more fibers sets were prepared. Electrospun (1) PET solution and (2) PET/$GdCl_3$ solution with Gd^{3+} : PET = 5:100 (wt: wt) and collected by aluminum plate, without NaOH/water reaction. All other parameters were the same as mentioned above for the other fibers. After electrospinning, these two samples, respectively named as PET and PET$GdCl_3$, were removed from the aluminum plate collector and dried 48 h in air at room temperature.

2.3 Animal experiments

The surgery was performed under sterile conditions. Fibrous membranes were firstly rolled up to about 1.5 cm length and 2 mm diameter cylinders. Each cylinder was subcutaneously implanted into the left-back site of 5 rats (from Medical Experimental Animal Center of Guangdong Province). PET-NaOH fibrous cylinders were also subcutaneously implanted into the right-back site of all rats as controls. The depth of implantation is about 5 mm beneath the skin. MRI examinations were carried on the 1st, 5th, 8th, 14th, 26th, 51st days after implantation (anesthesia with pentobarbital). All rats lived in a sterile condition. No dietary restrictions and fasting protocols were applied before and after implantation. Spleen, lungs, liver, kidneys and heart of each rat were harvested at the time of sacrifice after final MRI examination. Then these organs were embedded in paraffin, sectioned and hematoxylin/eosin (HE) stained for observation under optical microscope (Zeiss, Germany).

All animal experiments were approved by the Institutional Animal Care and Use Committee of South China University of Technology (SCUT, AEC No. 2020048) and carried out in compliance with the Care and Use of Laboratory Animals.

2.4 Characterization

Scanning electron microscopy (SEM) was performed on a Phenom Pro G3 (backscattering electron detector, Phenom, Holland). Samples were firstly coated with a layer of platinum by ion sputter (Q150T ES PLUS, Quorum, U.K.).

Transmission electron microscopy (TEM) was performed by firstly embedding samples in epoxy resin. Then they were ultrathin sliced by microtome (EM UC7/FC7, Leica, Austria). Slices were moved to 400-mesh copper grids and observed under TEM (JEM-F200, JEOL, Japan) at 200 kV. TEM images were Fourier transformed by ImageJ to observe the distribution of $Gd(OH)_3$. The brightness of the Fourier transformed images has been enhanced for convenient observation.

MRI was operated on an Ingenia 3.0T (Philips, Netherlands) with sequence parameters: T_1WI inverse recovery, TE = 20 ms, TR = 2045 ms, TI = 800 ms, and 0.65 mm × 0.81 mm voxel with 4 mm slice thickness; T_2WI turbo spin echo (TSE), TE = 105 ms, TR = 3000 ms, TSEes/shot = 7.8/171 ms and 0.3 mm × 0.3 mm voxel with 1 mm slice thickness. *In vitro* MRI was performed by bathing fibers in glass bottles filled with water (illustrated in Supporting Information Fig. S1).

Low field nuclear magnetic resonance (LFNMR) was performed on an MQ20 (Brooke, Germany) at 37 °C. Fibers were firstly soaked full of water and then filled in the tubes designed for LFNMR. Free water was poured out to guarantee all LFNMR signal came from water molecules that had saturated, and were physically bound to, the fibers. Samples were left for 10 minutes in the machine to reach thermal equilibrium before testing.

The evaluation of free Gd^{3+} ions' contribution on accelerating relaxation time was performed by soaking 0.1 g of fibers in 100 mL deionized water. 1 mL of water solution were taken after 3h, 6h, 12h, 1d, 2d, 4d, 7d, 15d, 30d, and 60d to test their T_1 relaxation times on LFNMR, where T_1 relaxation time of water molecules is sensitive to Gd^{3+} concentration. The standard curves (T_1 and T_2 relaxation time vs. concentration) of water/Gd^{3+} solutions were established by testing standard $GdCl_3$ solutions (Supporting Information Fig. S2a).

All samples were cut into dumbbell-like splines according to international standard ISO 527-3:2018(E) (Supporting Information Fig. S3) and performed at a rate of 50 mm/min on a mechanical stretching machine (LD22.102, ShenZhen Lanbosansi Material testing Co., Ltd, China).

Human umbilical vein endothelial cells (HUVEC-94 cell line, RRID:CVCL_A4BB, from ScienCell) were cultured in an incubator (Thermo Fisher, U.S.A.) with 5% carbon dioxide and humidified atmosphere. 0.1 g of all samples were firstly irradiated with ultraviolet (UV) light overnight. Then, the HUVECs were seeded in 96-well culture plates at a density of 1.0×10^4 cells per well and cultured for 24 h. Sample-soaked cell culture medium with 0.2 mL were then added and cultured. After 24 and 48 h culture, CCK-8 was added for *in vitro* cell viability assay according to its product instructions. Optical density (OD) was tested on a Spectra Max iD3 (Molecular Devices, USA). Cell viability was calculated as:

$$Cell viability = \left(OD_{Sample} - OD_{CCK-8}\right)/\left(OD_{Blank} - OD_{CCK-8}\right) \quad (1)$$

where OD_{sample} is the absorbance of the solution with sample-soaked cell culture medium, cells, and CCK-8; OD_{Blank} is the absorbance of the solution with pristine cell culture medium, cells, and CCK-8, and $OD_{CCK\text{-}8}$ is the absorbance of the solution with pristine cell culture medium and CCK-8.

Thermogravimetric analysis (TGA) was operated on TGA 5500 (TA Instruments, USA). Samples were heated from 30 °C to 700 °C at 10 °C/min in a nitrogen atmosphere.

X-ray diffraction (XRD) was tested on SmartLab SE (Rigaku, Japan) with copper target (λ = 1.5405 Å). Scanning 2θ from 10° to 60° at 5°/min.

Magnetization curves were obtained from a vibrating sample magnetometer (EverCool II, Quantum Design, USA) at 37 °C. Samples were magnetized in an external magnetic field from 0 to 50,000 Oe and then demagnetized down to 0 Oe at a rate of 200 Oe/s.

3 Results and discussion

All fibers electrospun in this study are listed in Table 1 to show the various conditions used to fabricate the systems in this work.

3.1 Morphology of fibers

PET-NaOH and PET/Gd fibers were successfully fabricated via electrospinning (see Supporting Information Fig. S4). PET-NaOH fibers were cylindrical with 1.58 ± 0.15 μm average diameter. With the addition of $GdCl_3$ to the spinning solution, and thus introduction of $Gd(OH)_3$ to the fibers, the fiber diameter decreased, where low loadings (PET/Gd0.1 ~ PET/Gd2) still

produced uniform fibers with smooth surface. The decrease in diameter might be caused by introducing more $GdCl_3$.Many studies have [61–63] reported the increased conductivity of spinning solution and decreased fiber diameter because of adding more inorganic salts. At higher $Gd(OH)_3$ contents, the fiber diameter decreased further, down to 0.59 ± 0.12 μm for the highest loading (PET/Gd5, as shown in Fig. 1c). Uneven nodular fibers were observed for higher $Gd(OH)_3$ contents (PET/Gd3 and PET/Gd5), indicating the decrease of electrospinnability for such high salt contents.

Magnetization and demagnetization curves (Supporting Information Fig. S9) of fibers confirmed the successful loading of Gd atoms in PET fibers. All PET/Gd fibers were paramagnetic.

3.2 $Gd(OH)_3$ distribution in fibers

XRD patterns (Supporting Information Fig. S8) of all fibers show that PET were amorphous. TEM images (Fig. 2a1-a4) show that $Gd(OH)_3$ nanoparticles were well distributed in PET matrix at low Gd loadings. As more $GdCl_3$ was incorporated into the spinning solution, small regions of regularly arranged $Gd(OH)_3$ nanoparticles were observed, as shown in the PET/Gd0.5 fiber slice (Fig. 2a2 red arrow). On increasing $GdCl_3$ loading further, larger areas of clusters with regularly arranged $Gd(OH)_3$ crystals were observed (see PET/Gd1, Fig. 2a3). Finally, in the fibers with the highest loading, PET/Gd5, $Gd(OH)_3$ aggregated to create larger spherical particles of tens of nanometers in diameter (Fig. 2a4). The interplanar spacing of the regular pattern within the aggregates was measured as approximately 0.34 nm, which is close to the 110 plane distance of $Gd(OH)_3$ crystal [64]. This indicated that $Gd(OH)_3$ in fibers (PET/Gd0.1 to PET/Gd0.3) were loosely arranged and well-dispersed in PET matrix. The transition of $Gd(OH)_3$ aggregates from totally amorphous and well-dispersed to partially crystalline aggregated clusters was also confirmed by Fourier transform analysis of the TEM images. In short, TEM results indicate that, via *in situ* reaction electrospinning, $Gd(OH)_3$ was successfully distributed at sub-nanometer length scales when no more than 0.3 g Gd (per hundred g PET) were loaded into the PET matrix.

3.3 Relaxation time and relaxivity

The T_1 and T_2 relaxation times of water molecules are the key factors for MRI signal intensity [37]. The T_1 and T_2 relaxation time reduction effect of CAs can be described by Eq 2

$$\frac{1}{T_i} = \frac{1}{T_{i0}} + r_i \cdot [CA] \; i = 1 \; or \; 2 \tag{2}$$

Where T is the relaxation time, r is the relaxivity, $[CA]$ is the concentration of CAs and T_{i0} is the relaxation time at $[CA] = 0$. Typically, CAs with higher relaxivity will generate higher MRI signal contrast.

It should be noted that traditional MRI CAs are fabricated to be water-soluble and tested in aqueous solution, and, according to Eq 2, the common units of relaxation time, $[CA]$ and relaxivity are s, mmol L^{-1}, and L $mmol^{-1}$ s^{-1}, respectively. In this study, $Gd(OH)_3$ has been dispersed in PET rather than water. Therefore, mmol g^{-1} (Gd^{3+}/PET) and g $mmol^{-1}$ s^{-1} are more relevant as the units of $[CA]$ and relaxivity, respectively. LFNMR test results are shown in Fig. 2c. Both T_1 and T_2 relaxation rates were proportional to $[CA]$ with a transition point at a critical concentration somewhere between PET/Gd0.5 and PET/Gd1. The T_1 and T_2 relaxivities were r_{1L} = 851.18 g $mmol^{-1}$ s^{-1} and r_{2L} = 80.87 g $mmol^{-1}$ s^{-1} at low concentration and r_{1H} = 24.89 g $mmol^{-1}$ s^{-1} and r_{2H} = 29.03 g $mmol^{-1}$ s^{-1} at high concentration. This transitional concentration coincides with the change in aggregation state (amorphous to crystalline) observed in TEM images and indicated that well-dispersed $Gd(OH)_3$ clusters (sub-nano scale) had greater than 34 times higher T_1 relaxivity than aggregated (crystalline) ones. We attribute this finding to increased surface area. According to SBM theory [50,51], when more Gd atoms are accessible in well-dispersed $Gd(OH)_3$ (than those buried within larger aggregated clusters) they are better at coordinating with water molecules, which leads to a higher T_1 relaxivity (Fig. 2b). In other words, this strategy of exposing more metal atoms on the aggregates' surface allows more effective coordination with water molecules, which was previously proved to be an effective approach for enhancing water-soluble IONP T_1 contrast [65]. In our work, this strategy has clearly been successful for $Gd(OH)_3$ embedded within PET matrix.

In order to compare the relaxivity of $Gd(OH)_3$ embedded in fibers and dissolved in water, 1.38 g cm^{-3} was used as PET density (reported as 1.34 to 1.40 g cm^{-3} depending on the form [66]) to convert the units of r_1 and r_2 to L $mmol^{-1}$ s^{-1}. This gave values of r_{1L} = 1.175 g $mmol^{-1}$ L^{-1}, r_{1H} = 0.112 g $mmol^{-1}$ L^{-1}, r_{2L} = 0.034 g $mmol^{-1}$ L^{-1} and r_{2H} = 0.040 g $mmol^{-1}$ L^{-1}. It can be seen that the r_1 values of well-dispersed $Gd(OH)_3$ in fibers are only 9.55% of those dissolved in water (r_1 = 12.3 L $mmol^{-1}$ s^{-1}) [57]. This indicated that only a small portion of $Gd(OH)_3$ (*i.e.* those that were distributed on the surface of fibers) could coordinate with water molecules and speed up their relaxation. Others were trapped within the PET chains, limiting their efficacy.

3.4 In vitro *MRI*

LFNMR results proved that PET/Gd fibers could accelerate T_1 and T_2 water relaxation times. Subsequently, the composite fibers were immersed in water to test their MRI contrast effects. As shown in Fig. 3 a1, water and PET-NaOH fibers both exhibit low signal intensity. T_1WI signal intensity was seen to increase with increasing $Gd(OH)_3$ concentration, as expected. Water has an inherently high signal intensity under T_2WI (Fig. 3a2). PET-NaOH fibers immersed in water showed similar signal intensity to water, which indicated that PET provided no MRI contrast. Conversely, all PET/Gd fibers showed negative contrast. The uneven signal intensity of fibrous samples in both (a1) and (a2) was caused by uneven filling density of fibers, since fibers expelled water molecules and caused a decrease in water density where fibers were. Fiber outline and shape could be clearly imaged, as shown in Fig. 3b.

3.5 The influence of free Gd^{3+} ions

Although $Gd(OH)_3$ has very low solubility in water ($k_{sp} = 8.2 \times 10^{-23}$) [58], the existence of free Gd^{3+} is inevitable. Accelerated relaxation caused by free Gd^{3+} should therefore be evaluated. The T_1 relaxation times of the water used to bathe PET/Gd and PET/$GdCl_3$ fibers were measured, as shown in Fig. 3 e1. For PET/Gd fibers, the T_1 relaxation times of water

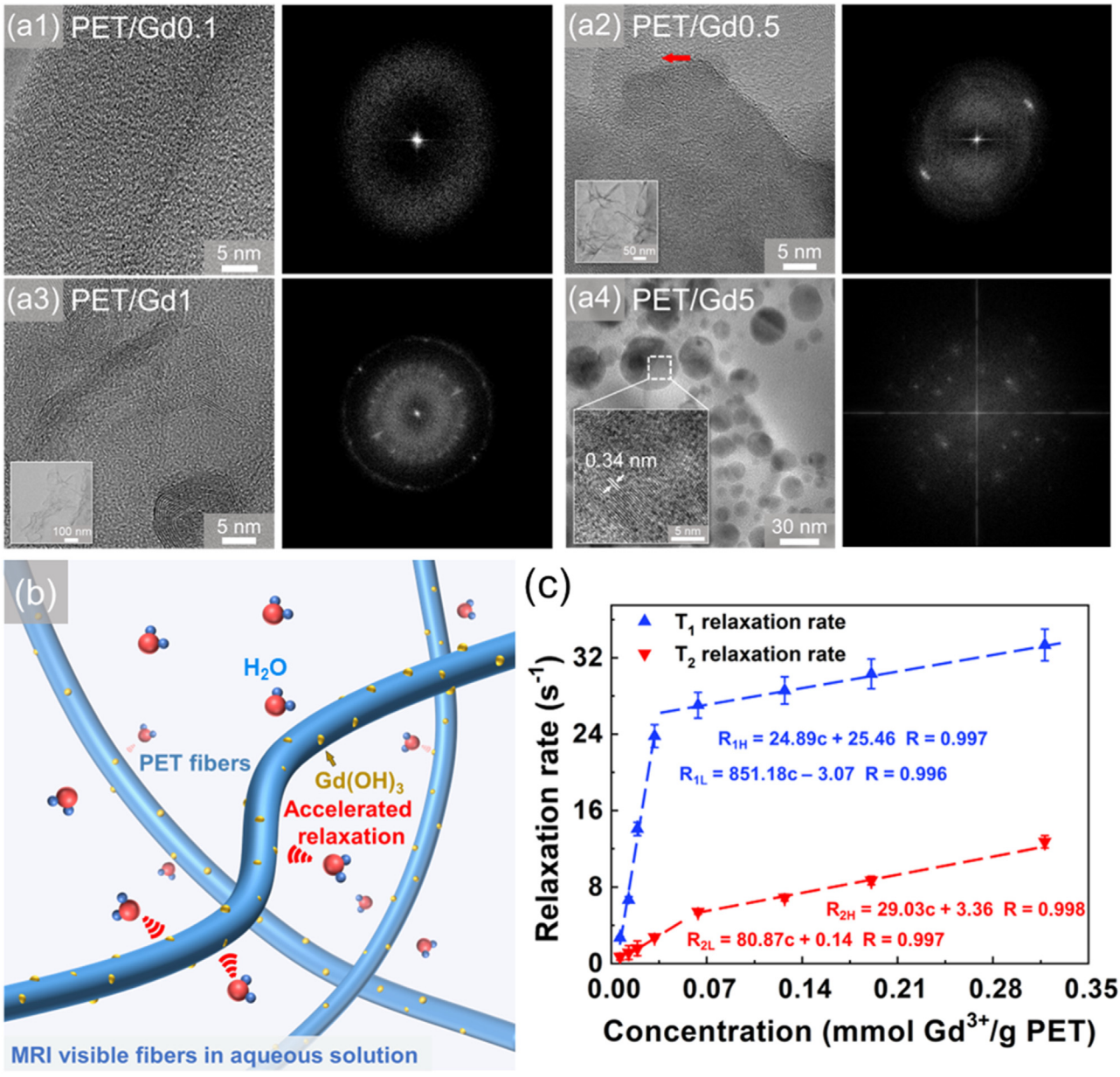

Fig. 2

High resolution TEM images of PET/Gd fibers (a1-a4) and corresponding Fourier transform images. The brightness of the Fourier transformed images has been enhanced for convenient observation. (b) Well-dispersed $Gd(OH)_3$ accelerated the relaxation time of surrounding water molecules that saturated the fibers. (c) T_1 and T_2 relaxation rates (reciprocal of relaxation time) of water adjacent to the PET/Gd fibers (PET/Gd0.1 to PET/Gd5 fibers from left to right). Average and standard deviation values are produced by LFNMR.

decreased from about 3800 ms (pure water) to a minimum of 3182 ms, which indicated that more Gd^{3+} ions were dissolved in water with time. However, this 'relaxation acceleration' from Gd^{3+} was much smaller than the overall effect contributed by PET/Gd fibers. As shown in Fig. 2c, the relaxation rates (inverse of relaxation time) of PET/Gd0.1 and PET/Gd5 fibers were 2.70 s^{-1} and 33.33 s^{-1} (i.e., the relaxation times were 370 ms and 30 ms). This result indicated that the relaxation acceleration effect of PET/Gd fibers was mainly provided by $Gd(OH)_3$ rather than free Gd^{3+}. PET/$GdCl_3$ fibers were also tested to illustrate the rapid release of water-soluble $GdCl_3$.

The relationship between the relaxation time of water and dissolved Gd^{3+} concentration can be described by Eq2. Thus, the relaxation time *versus* concentration standard curve of $GdCl_3$/water solution were plotted (Supporting Information Fig. S2a) to calculate the Gd^{3+} concentration in the water used to bathe PET/Gd and PET/$GdCl_3$ fibers (Fig. 3e2 and e3). For all fibers, Gd^{3+} concentration rose quickly in the first 7 days and soon reached a plateau. PET/Gd0.1 to PET/Gd2 fibers showed nearly the same Gd^{3+} plateau concentration (which is the saturation concentration of $Gd(OH)_3$) and released the same amount of Gd^{3+} after 60 days of study (see released amount in Fig. S2b).

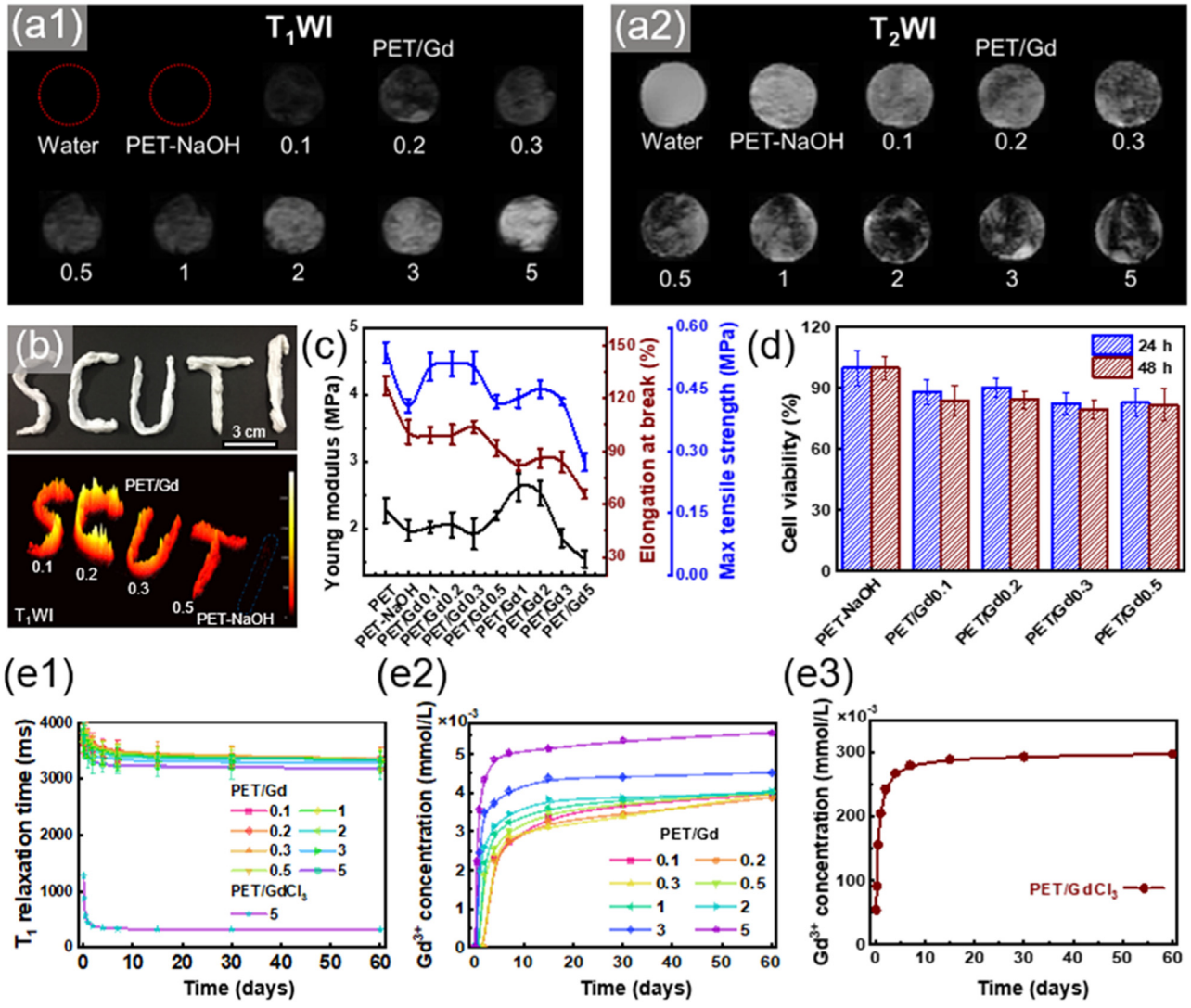

Fig. 3

In vitro MRI T_1WI (a1) and T_2WI (a2) images of pure water, PET-NaOH and PET/Gd fibers immersed in water. (b) Outline resolution test of PET/Gd fibers. (c) Tensile test results, where multiple measurements were recorded to obtain 5 valid results. (d) Cell viability after 24h and 48h culture (3 parallel tests for each sample). (e1) T_1 relaxation time and Gd concentration (e2 and e3) of the water used to bathe the fibers (e2 and e3).

PET/Gd3 and PET/Gd5 fibers showed higher release equilibrium concentrations than the other fibers, indicating that when too much (≥ 3% wt.) $GdCl_3$ was loaded into the PET fibers, there was incomplete reaction of $GdCl_3$ with NaOH. TGA analysis (Supporting Information Fig. S7 h and j) of PET/Gd3 and PET/Gd5 fibers showed that a $GdCl_3{\cdot}H_2O$ thermal decomposition peak could be observed and provided further evidence for the incomplete reaction.

3.6 Tensile properties

Undesirable mechanical properties will dramatically limit the future application of PET/Gd fibers. Thus, mechanical stretching was performed to test the influence of the NaOH reaction and the addition of $Gd(OH)_3$ (Fig. 3c) on the tensile properties of the new materials. By comparing PET and PET-NaOH fibers, it can be seen that the presence of NaOH reduced both Young modulus and elongation at break. This is attributed to the partial degradation of PET under such alkaline conditions [67,68]. Gd has a good affinity to oxygen [69], which may enhance the bonding at $Gd(OH)_3$ - PET interfaces. However, loading overly large nanoparticles into the polymer matrix may introduce concentrated regions of stress [70]. It is proposed that these two factors together led to the initial rise and then fall in the Young's modulus of the PET/Gd fibers with increasing concentration of $Gd(OH)_3$. Additionally, this work and previous studies [71,72] all show that smaller diameter fibers of the same material tend to exhibit lower elongation at break. Generally speaking, low $Gd(OH)_3$ loadings (PET/Gd0.1 to PET/Gd 0.5) showed no detrimental decrease in tensile properties.

3.7 Cell viability

Biosafety is an essential element for biomedical application and needs to be studied. Based on the above studies, PET/Gd1

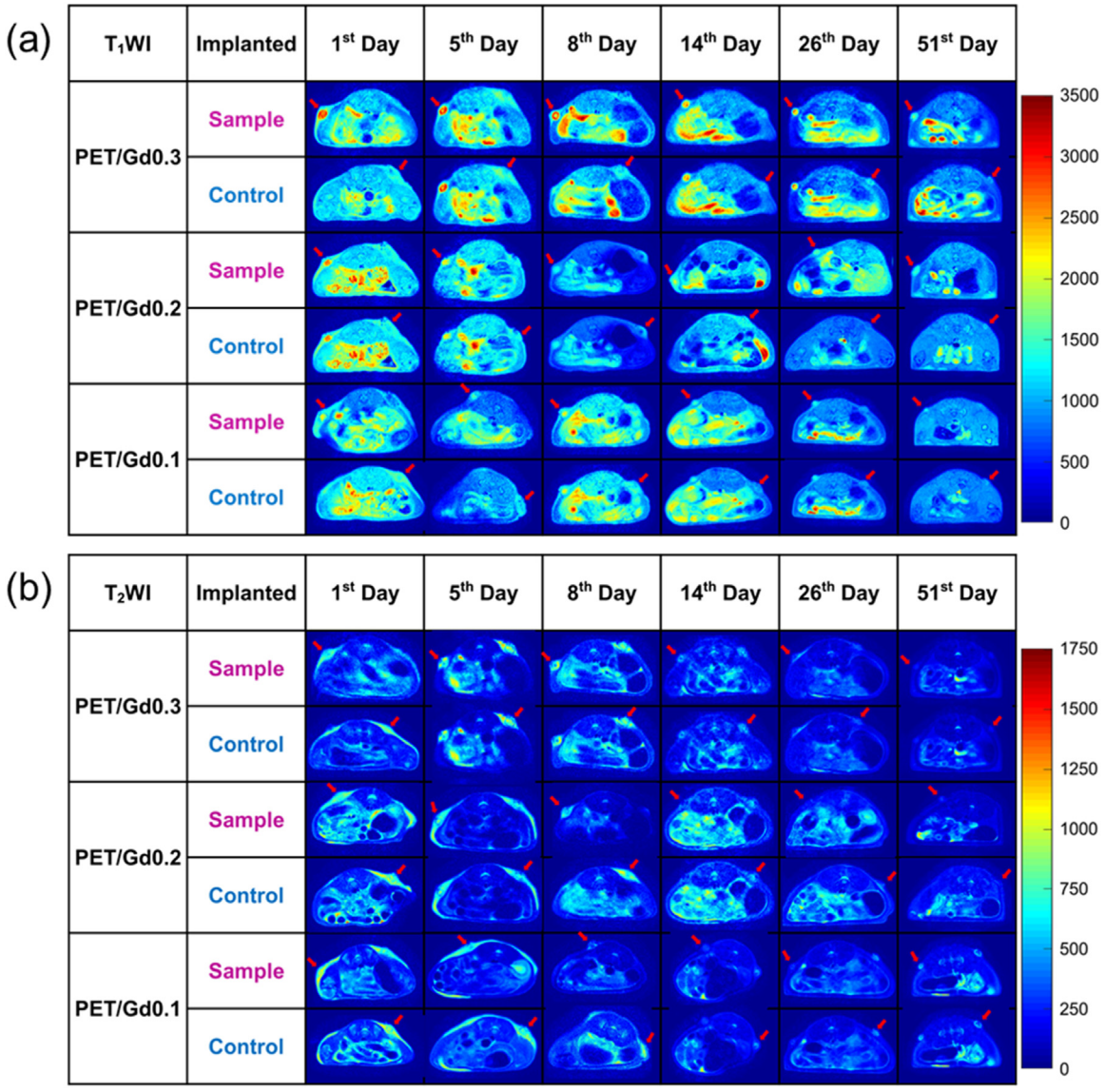

Fig. 4

In vivo MRI T_1WI (a) and T_2WI (b) images of PET/Gd (sample) and PET-NaOH (control) fibers.

to PET/Gd5 fibers showed low relaxivity, higher free Gd^{3+} concentration and a dramatic negative effect on tensile properties. In short, these samples were comprehensively poor in performance and were not suitable for further study. Thus, the biocompatibility of PET-NaOH and other PET/Gd fibers (PET/Gd0.1 to PET/Gd0.5) were assessed. The results (Fig. 3d) revealed that loading low concentration $Gd(OH)_3$ in PET fibers did not show obvious cytotoxicity.

3.8 Animal studies

Gd^{3+} is highly toxic [73] and should be used at a minimal dosage. Thus, the three fibrous systems with the lowest $Gd(OH)_3$ content were implanted to assess their imaging ability and biosafety. PET-NaOH fibers were also implanted as controls. Representative transverse cross-sections of *pseudo*-colored MR images are listed and arrows indicate the PET/Gd (sample) and PET-NaOH fibers (control) in Fig. 4. Limited by the accuracy of surgery and MRI scanning, in some cases, samples and controls were in different cross-sections and are therefore shown separately. The absolute signal intensity of samples, controls and adjacent tissue in MR images were collected and are illustrated in Fig. 5a1-a3 and b1-b3.

Under a T_1WI sequence (Fig. 4a), all PET/Gd fiber outlines and positions can be clearly observed. Meanwhile, controls showed a similar signal intensity to adjacent tissue and could not be readily distinguished from the environment. Among them, PET/Gd0.3 fibers delivered the highest contrast. The signal intensity of all samples decreased over time, getting closer to the adjacent tissue throughout the course of the study (as shown in Fig. 5a1–a3). Controls and adjacent tissue consistently showed similar signal intensity which indicated that the signal of the control was not provided by PET but by the environment (such as bodily fluid). Generally, PET/Gd fibers showed good positive contrast.

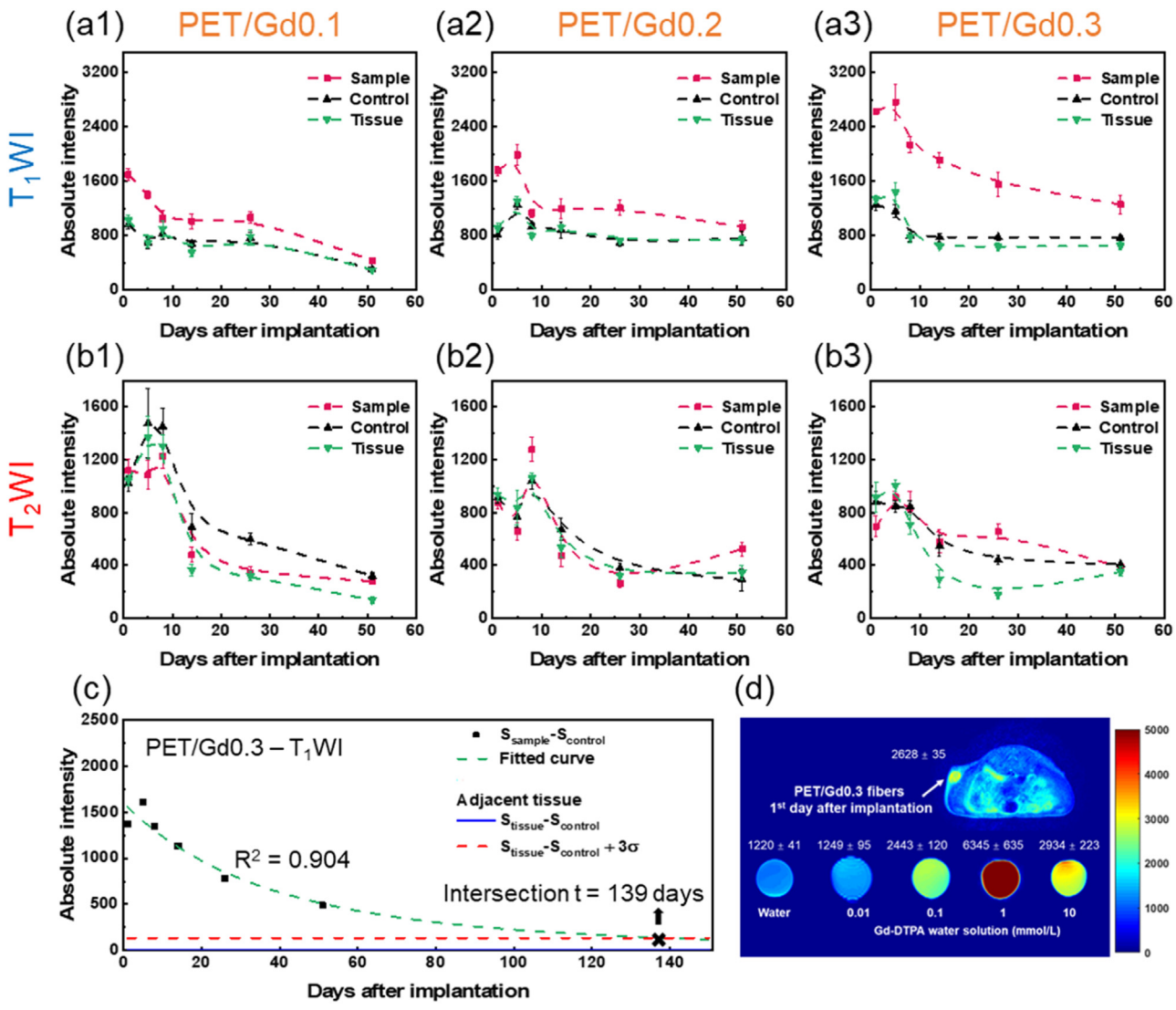

Fig. 5

Statistical signal intensity of *in vivo* MRI T_1WI (a1-a3) and T_2WI (b1-b3) images. Signal intensity of tissue around fibers were also collected. 10 data points were evenly selected along the diameter direction of samples and controls to calculate average signal intensity and standard deviation. (c) Curve fitting of PET/Gd0.3 fiber MRI T_1WI image signal intensity and estimated imaging lifetime. (d) Comparison with commercial CA under T_1WI (concentration and absolute signal intensity marked).

Under a T_2WI sequence, the signal intensity of samples, controls, and adjacent tissue were higher at an early stage and decreased with time (as shown in Fig. 5b1–b3). This phenomenon was caused by edema due to surgery as water molecules could offer high signal intensity in T_2WI. Adjacent tissue edema can also be found in T_1WI, but as the water molecules provide relatively low signal intensity in T_1WI, the signal from the PET/Gd fibers was still high enough to be distinguished from the environment. Thus, it can be deduced that the sample and control signal intensities in T_2WI were largely affected by water molecule density. Meanwhile, T_2WI negative contrast of PET/Gd fibers was not found.

After MRI examination, rat spleens, lungs, livers, kidneys and hearts were HE stained and observed under an optical microscope. No obvious change in cell morphology was found (Supporting Information Fig. S5) which supported PET/Gd0.1 ~ PET/Gd0.3 fibers' long-term biosafety.

The signal intensity of PET/Gd0.3 fibers (highest positive contrast) was fitted to calculate their imaging lifetime (as shown in Fig. 5c). See fitting method described in the Supporting Information. When the fiber signal intensity dropped to the average signal intensity of the adjacent tissue (plus 3 times the standard deviation), the signal contrast was deemed not high enough to distinguish fibers from the environment. The fitting results suggested that PET/Gd0.3 can be observed up to 139 days. This long-term visibility endows PET/Gd0.3 fibers with good prospect to be further used in biomedical applications, such as tissue engineering scaffoldings, patches for brain, intestine, heart etc. A more realistic clinically relevant animal model is deserved for better future application.

MRI signal intensity is the key to identify fibers from the environment. Gd-DTPA is widely used as positive CA and brings ideal contrast for assisting MRI diagnosis. Therefore, Gd-

DTPA was prepared in standard solutions (Fig. 5d) as signal intensity criterion to evaluate the PET/Gd0.3 fibers' contrast effect. According to the Gd-DTPA instruction manual, no less than 0.1 mmol Gd-DTPA per kilogram body weight is recommended to be injected. In the first day after implantation, PET/Gd0.3 fibers showed higher signal intensity than the 0.1 mmol/L Gd-DTPA solution, which indicated its good imaging performance. Taking a 60 kg adult as an example, the Gd dosage used in per gram PET/Gd0.3 fibers (3 mg) was only 0.32% (3/943.5 × 100%) of the MRI scan assisted by injecting Gd-DTPA (943.5 mg Gd dosage), which indicated the low biosafety risk of our systems. The reason why such low Gd dosage is needed in PET matrix is that Gd-DTPA is water-soluble and will spread throughout the body after injection. In conventional systems, high Gd-DTPA dosage is needed to maintain a suitable concentration, whereas here, $Gd(OH)_3$ is fabricated in a high relaxivity state (well-dispersed) and trapped inside PET fibers. Even at low dosage, its contrast is sufficient to highlight PET fibers under MRI.

It can be concluded that *in vivo* MRI signals come from many substances, such as water molecules, background noise, etc. and the sum of the signals fluctuates around an average value. If a CA, like $Gd(OH)_3$, has a low T_2 relaxivity, its small T_2 negative contrast might be covered by high-intensity signal sources (like T_2WI signal fluctuation caused by an edema in this work). Combining the LFNMR and *in vivo* MRI results, we suspected that the reason why IONPs and ferritin have failed to provide positive contrast in previous studies is that those nanoparticles were not well-dispersed within the polymer matrix. T_1 relaxivity significantly decreases due to aggregation and cannot be observed out of background noise under *in vivo* MRI conditions and only T_2 contrast remains.

4 Conclusion

Electrospun MRI-active nanofibers endowed with long-term positive contrast have been fabricated by embedding a well-dispersed CA. The crucial new step involved the *in situ* reaction of $GdCl_3$ with NaOH during electrospinning to successfully fabricate PET fibers loaded with $Gd(OH)_3$. The effect of $Gd(OH)_3$ aggregation, from a well-dispersed amorphous state to larger aggregates of tens of nanometers in size, was studied. TEM and LFNMR results showed that well-dispersed $Gd(OH)_3$ (sub-nanometer size) in PET fibers had 34 times higher T_1 relaxivity than aggregated ones. With only 0.3 wt% Gd loading (compared to polymer; PET/Gd0.3) our nanofibers were shown to not only provide excellent T_1 positive contrast (close to commercial Gd-DTPA) with approximately 139 days of imaging lifetime, but also possess good balanced performance in terms of relaxivity, tensile properties, and biosafety (only 0.32% Gd dosage compared with commercial MRI CA, Gd-DTPA). As *in vivo* studies showed, MRI signals came from multiple sources. The imaging effect of a CA with low relaxivity would be covered up by other high signal sources. Good dispersion and full coordination with water molecules are shown to be crucial for CAs in maintaining their high T_1 relaxivity within a polymer matrix and guaranteeing the MRI quality of electrospun fibers. Despite the known good properties of this proof-of-concept system, future investigation on a more realistic and clinically relevant model is required as the next step for improving the MRI-active feasibility of future fibrous materials.

In summary, the excellent properties of PET/Gd0.3 fibers revealed a new fabrication route for materials with long-term MRI positive contrast for potential biomedical application. The versatile *in situ* synthesis during electrospinning shows tremendous promise for visualizing various types of polymers in MRI technology.

Author contributions

Yifan Jia: Conceptualization, Data curation, Formal analysis, Methodology, Writing – original draft; Weiwen Yuan: Formal analysis, Investigation, Validation; Mengmeng Xu: Data curation, Investigation, Validation; Congyi Yang: Investigation, Validation; Lei Chen: Investigation; Shuo Wang: Investigation; Paul D. Topham: Writing – review & editing; Guoxuan Luo: Investigation; Mo Wang: Investigation; Yong Zhang: Conceptualization, Funding acquisition, Methodology; Guihua Jiang: Conceptualization, Formal analysis, Methodology; Qianqian Yu: Conceptualization, Data curation, Formal analysis, Funding acquisition, Methodology, Supervision, Writing – original draft; LinGe Wang: Conceptualization, Data curation, Formal analysis, Funding acquisition, Methodology, Supervision, Validation, Writing – review & editing.

Declaration of competing interests

The authors declare that they have no known competing financial interests or personal relationships that could have appeared to influence the work reported in this paper.

Data Availability

Data will be made available on request.

Acknowledgements

The authors thank the financial support from the National Key R&D Program of China (No. 2017YFC1105003), Guangdong Project (No. 2016ZT06C322), Overseas Expertise Introduction Center for Discipline Innovation ("111 Center"), Science and Technology Program of Guangzhou (No. 202102020759), and Science Foundation of Guangdong Second Provincial General Hospital (No. 3D-B2020010).

Supplementary materials

Supplementary material associated with this article can be found, in the online version, at doi:10.1016/j.giant.2022.100121.

References

[1] M.N. Collins, G. Ren, K. Young, S. Pina, R.L. Reis, J.M. Oliveira, Scaffold fabrication technologies and structure/function properties in bone tissue engineering, Adv. Funct. Mater. 31 (2021) 2010609, doi:10.1002/adfm.202010609.

[2] X. Zhao, X. Chen, H. Yuk, S. Lin, X. Liu, G. Parada, Soft materials by design: unconventional polymer networks give extreme properties, Chem. Rev. 121 (2021) 4309–4372, doi:10.1021/acs.chemrev.0c01088.

[3] A. Melvin, A. Litsky, J. Mayerson, K. Stringer, D. Melvin, N. Juncosa-Melvin, An artificial tendon to connect the quadriceps muscle to the Tibia, J. Orth. Res. 29 (2011) 1775–1782, doi:10.1002/jor.21419.

[4] X. Wang, Y. Ding, H. Li, X. Mo, J. Wu, Advances in electrospun scaffolds for meniscus tissue engineering and regeneration, J. Biomed. Mater. Res. Part B - Appl. Biomater. 110 (2021) 923–949, doi:10.1002/jbm.b.34952.

[5] D. Chouhan, N. Dey, N. Bhardwaj, B.B. Mandal, Emerging and innovative approaches for wound healing and skin regeneration: current status and advances, Biomaterials 216 (2019) 119267, doi:10.1016/j.biomaterials.2019.119267.

[6] I. Jun, H.S. Han, J.R. Edwards, H. Jeon, Electrospun fibrous scaffolds for tissue engineering: viewpoints on architecture and fabrication, Int. J. Mol. Sci. 19 (2018) 745, doi:10.3390/ijms19030745.

[7] A. Wubneh, E.K. Tsekoura, C. Ayranci, H. Uludag, Current state of fabrication technologies and materials for bone tissue engineering, Acta Biomater 80 (2018) 1–30, doi:10.1016/j.actbio.2018.09.031.

[8] J.J. Xue, T. Wu, Y.Q. Dai, Y.N. Xia, Electrospinning and electrospun nanofibers: methods, materials, and applications, Chem. Rev. 119 (2019) 5298–5415, doi:10.1021/acs.chemrev.8b00593.

[9] F.J. Bye, L. Wang, A.J. Bullock, K.A. Blackwood, A.J. Ryan, S. MacNeil, Postproduction processing of electrospun fibres for tissue engineering, Jove-J. Visualized Exp. 66 (2012) e4172, doi:10.3791/4172.

[10] L. Chen, D. Zhang, K. Cheng, W.C. Li, Q.Q. Yu, L.G. Wang, Photothermal-responsive fiber dressing with enhanced antibacterial activity and cell manipulation towards promoting wound-healing, J. Colloid Interface Sci. 623 (2022) 21–33, doi:10.1016/j.jcis.2022.05.013.

[11] Y.P. Ding, W. Li, F. Zhang, Z.H. Liu, N.Z. Ezazi, D.F. Liu, H.A. Santos, Electrospun fibrous architectures for drug delivery, tissue engineering and cancer therapy, Adv. Funct. Mater. 29 (2019) 1802852, doi:10.1002/adfm.201802852.

[12] S.X. Chen, R.Q. Li, X.R. Li, J.W. Xie, Electrospinning: An enabling nanotechnology platform for drug delivery and regenerative medicine, Adv. Drug Del. Rev. 132 (2018) 188–213, doi:10.1016/j.addr.2018.05.001.

[13] S. Homaeigohar, A.R. Boccaccini, Antibacterial biohybrid nanofibers for wound dressings, Acta Biomater 107 (2020) 25–49, doi:10.1016/j.actbio.2020.02.022.

[14] K. Kalantari, A.M. Afifi, H. Jahangirian, T.J. Webster, Biomedical applications of chitosan electrospun nanofibers as a green polymer - review, Carbohydr. Polym. 207 (2019) 588–600, doi:10.1016/j.carbpol.2018.12.011.

[15] D.G. Yu, J.J. Li, G.R. Williams, M. Zhao, Electrospun amorphous solid dispersions of poorly water-soluble drugs: a review, J. Controlled Release. 292 (2018) 91–110, doi:10.1016/j.jconrel.2018.08.016.

[16] C. Cleeton, A. Keirouz, X.F. Chen, N. Radacsi, Electrospun nanofibers for drug delivery and biosensing, ACS Biomater. Sci. Eng. 5 (2019) 4183–4205, doi:10.1021/acsbiomaterials.9b00853.

[17] M. Radmansouri, E. Bahmani, E. Sarikhani, K. Rahmani, F. Sharifianjazi, M. Irani, Doxorubicin hydrochloride - Loaded electrospun chitosan/cobalt ferrite/titanium oxide nanofibers for hyperthermic tumor cell treatment and controlled drug release, Int. J. Biol. Macromol. 116 (2018) 378–384, doi:10.1016/j.ijbiomac.2018.04.161.

[18] S. Talebian, J. Foroughi, S.J. Wade, K.L. Vine, A. Dolatshahi-Pirouz, M. Mehrali, J. Conde, G.G. Wallace, Biopolymers for antitumor implantable drug delivery systems: recent advances and future outlook, Adv. Mater. 30 (2018) 1706665, doi:10.1002/adma.201706665.

[19] J. Zhao, W. Cui, Functional electrospun fibers for local therapy of cancer, Adv. Fiber Mater. 2 (2020) 229–245, doi:10.1007/s42765-020-00053-9.

[20] X.Y. Yang, K.Y. Li, X. Zhang, C. Liu, B.K. Guo, W.J. Wen, X.H. Gao, Nanofiber membrane supported lung-on-a-chip microdevice for anti-cancer drug testing, Lab Chip. 18 (2018) 486–495, doi:10.1039/c7lc01224a.

[21] L. Chen, Q. Yu, K. Cheng, P.D. Topham, M. Xu, X. Sun, Y. Pan, Y. Jia, S. Wang, L. Wang, Can photothermal post-operative cancer treatment be induced by a thermal trigger? ACS Appl. Mater. Interfaces. 13 (2021) 60837–60851, doi:10.1021/acsami.1c16283.

[22] C. Chen, Z. Wu, P. Ding, N. Sun, H. Liu, Y. Chen, Z. Wang, R. Pei, Peptide NGR modified TiO2 nanofiber substrate for circulating tumor cells capture, Adv. Fiber Mater. 2 (2020) 186–193, doi:10.1007/s42765-020-00040-0.

[23] D.S. Novikov, V.G. Kiselev, S.N. Jespersen, On modeling, Magn. Reson. Med. 79 (2018) 3172–3193, doi:10.1002/mrm.27101.

[24] L.D. Christiano, R. Singh, V. Sukul, C.J. Prestigiacomo, C.D. Gandhi, Microvascular decompression for trigeminal neuralgia: visualization of results in a 3D stereoscopic virtual reality environment, Minim. Invasive Neurosurg. 54 (2011) 12–15, doi:10.1055/s-0031-1273731.

[25] I. Rausch, A. Valladares, L.K.S. Sundar, T. Beyer, M. Hacker, M. Meyerspeer, E. Unger, Standard MRI-based attenuation correction for PET/MRI phantoms: a novel concept using MRI-visible polymer, Ejnmmi Physics 8 (2021) 18, doi:10.1186/s40658-021-00364-9.

[26] J. Otto, D. Busch, C. Klink, A. Ciritsis, A. Woitok, C. Kuhl, U. Klinge, U.P. Neumann, N.A. Kraemer, J. Conze, In vivo MRI visualization of parastomal mesh in a porcine model, Hernia 18 (2014) 663–670, doi:10.1007/s10029-014-1270-4.

[27] I. Urbankova, N. Sindhwani, G. Callewaert, A. Turri, R. Rinkijevic, L. Hympanova, A. Feola, J. Deprest, In vivo documentation of shape and position changes of MRI-visible mesh placed in rectovaginal septum, J. Mech. Behav. Biomed. Mater. 75 (2017) 379–389, doi:10.1016/j.jmbbm.2017.08.005.

[28] C. Zhang, J. Li, C. Yang, S. Gong, H. Jiang, M. Sun, C. Qian, A pH-sensitive coordination polymer network-based nanoplatform for magnetic resonance imaging-guided cancer chemo-photothermal synergistic therapy, Nanomed. Nanotechnol. Biol. Med. 23 (2020) 102071, doi:10.1016/j.nano.2019.102071.

[29] N.A. Kraemer, H. Donker, N. Kuehnert, J. Otto, C.K. Kuhl, In Vivo visualization of polymer-based mesh implants using conventional magnetic resonance imaging and positive-contrast susceptibility imaging, Invest. Radiol. 48 (2013) 200–205, doi:10.1097/rli.0b013e31827efd14.

[30] B. Zhang, Y. Gao, R. Yang, Z. Ouyang, H. Yu, H. Wang, X. Shi, M. Shen, Tumor-anchoring drug-loaded fibrous microspheres for mr imaging-guided local chemotherapy and metastasis inhibition, Adv. Fiber Mater. 10 (2022) e0120218, doi:10.1007/s42765-022-00137-8.

[31] G.K. Fletcher, L.D. Nash, L.M. Graul, L.K. Jang, S.M. Herting, M.D. Wilcox, T.J. Touchet, A.K. Sweatt, M.P. McDougall, S.M. Wright, D.J. Maitland, Chemical modifications of porous shape memory polymers for enhanced X-ray and MRI visibility, Molecules 25 (2020) 660, doi:10.3390/molecules25204660.

[32] R.A. Hamideh, B. Akbari, P. Fathi, S.K. Misra, A. Sutrisno, F. Lam, D. Pan, Biodegradable MRI visible drug eluting stent reinforced by metal organic frameworks, Adv. Healthcare Mater. 9 (2020) 2000136, doi:10.1002/adhm.202000136.

[33] M. Younis, V. Darcos, C. Paniagua, P. Ronjat, L. Lemaire, B. Nottelet, X. Garric, Y. Bakkour, J.H. El Nakat, J. Coudane, MRI-visible polymer based on poly(methyl methacrylate) for imaging applications, RSC Adv 6 (2016) 5754–5760, doi:10.1039/c5ra23646k.

[34] S. Blanquer, O. Guillaume, V. Letouzey, L. Lemaire, F. Franconi, C. Paniagua, J. Coudane, X. Garric, New magnetic-resonance-imaging-visible poly(epsilon-caprolactone)-based polyester for biomedical applications, Acta Biomater 8 (2012) 1339–1347, doi:10.1016/j.actbio.2011.11.009.

[35] J. Guo, X.Q. Jiang, C.Z. Yang, Polymeric gadolinium chelate-containing magnetic resonance signal-enhancing coating materials: synthesis, characterization, and properties, J. Appl. Polym. Sci. 87 (2003) 1358–1364, doi:10.1002/app.11428.

[36] Y. Jia, C. Yang, X. Chen, W. Xue, H.J. Hutchins-Crawford, Q. Yu, P.D. Topham, L. Wang, A review on electrospun magnetic nanomaterials: methods, properties and applications, J. Mater. Chem. C. 9 (2021) 9042–9082, doi:10.1039/D1TC01477C.

[37] R.H. Hashemi, W.G. Bradley, C.J. Lisanti, MRI : The Basics, Lippincott Williams & Wilkins, Philadelphia, USA, 2010.

[38] H. Awada, S. Sene, D. Laurencin, L. Lemaire, F. Franconi, F. Bernex, A. Bethry, X. Garric, Y. Guari, B. Nottelet, Long-term in vivo performances of polylactide/iron oxide nanoparticles core-shell fibrous nanocomposites as MRI-visible magneto-scaffolds, Biomater. Sci. 9 (2021) 6203–6213, doi:10.1039/d1bm00186h.

[39] H. Zhang, J. Xia, X. Pang, M. Zhao, B. Wang, L. Yang, H. Wan, J. Wu, S. Fu, Magnetic nanoparticle-loaded electrospun polymeric nanofibers for tissue engineering, Mater. Sci. Eng. C Mater. Biol. Appl. 73 (2017) 537–543, doi:10.1016/j.msec.2016.12.116.

[40] M.K. Shin, S.I. Kim, S.J. Kim, S.Y. Park, Y.H. Hyun, Y. Lee, K.E. Lee, S.-S. Han, D.-P. Jang, Y.-B. Kim, Z.-H. Cho, I. So, G.M. Spinks, Controlled magnetic nanofiber hydrogels by clustering ferritin, Langmuir 24 (2008) 12107–12111, doi:10.1021/la802155a.

[41] E.G. Walsh, D.R. Mills, S. Lim, B. Sana, K.E. Brilliant, W.K.C. Park, MRI contrast demonstration of antigen-specific targeting with an iron-based ferritin construct, J. Nanopart. Res. 15 (2013) 1409, doi:10.1007/s11051-012-1409-0.

[42] E.A. Neuwelt, B.E. Hamilton, C.G. Varallyay, W.R. Rooney, R.D. Edelman, P.M. Jacobs, S.G. Watnick, Ultrasmall superparamagnetic iron oxides (USPIOs): a future alternative magnetic resonance (MR) contrast agent for patients at risk for nephrogenic systemic fibrosis (NSF)? Kidney Int 75 (2009) 465–474, doi:10.1038/ki.2008.496.

[43] E. Taboada, E. Rodriguez, A. Roig, J. Oro, A. Roch, R.N. Muller, Relaxometric and magnetic characterization of ultrasmall iron oxide nanoparticles with high magnetization. Evaluation as potential T-1 magnetic resonance imaging contrast agents for molecular imaging, Langmuir 23 (2007) 4583–4588, doi:10.1021/la063415s.

[44] N. Talebloo, M. Gudi, N. Robertson, P. Wang, Magnetic particle imaging: current applications in biomedical research, J. Magn. Reson. Imaging. 51 (2019) 1659–1668, doi:10.1002/jmri.26875.

[45] D.R. Zhu, F.Y. Liu, L.N. Ma, D.J. Liu, Z.X. Wang, Nanoparticle-based systems for T-1-weighted magnetic resonance imaging contrast agents, Int. J. Mol. Sci. 14 (2013) 10591–10607, doi:10.3390/ijms140510591.

[46] M. Jin, D.G. Yu, X. Wang, C. Geraldes, G.R. Williams, S.W.A. Bligh, Electrospun contrast-agent-loaded fibers for colon-targeted MRI, Adv. Healthcare Mater. 5 (2016) 977–985, doi:10.1002/adhm.201500872.

[47] A.Y. Darwesh, M.S. El-Dahhan, M.M. Meshali, New oral coaxial nanofibers for gadodiamide-prospective intestinal magnetic resonance imaging and theranostic, Int. J. Nanomed. 15 (2020) 8933–8943, doi:10.2147/ijn.s281158.

[48] V.S. Vexler, O. Clement, H. Schmitt-Willich, R.C. Brasch, Effect of varying the molecular weight of the MR contrast agent Gd-DTPA-polylysine on blood pharmacokinetics and enhancement patterns, J. Magn. Reson. Imaging. 4 (1994) 381–388, doi:10.1002/jmri.1880040325.

[49] P. Joffe, H.S. Thomsen, M. Meusel, Pharmacokinetics of gadodiamide injection in patients with severe renal insufficiency and patients undergoing hemodialysis

or continuous ambulatory peritoneal dialysis, Acad. Radiol. 5 (1998) 491–502, doi:10.1016/s1076-6332(98)80191-8.

[50] R.B. Lauffer, Paramagnetic metal complexes as water proton relaxation agents for NMR imaging: theory and design, Chem. Rev. 87 (1987) 901–927, doi:10.1021/cr00081a003.

[51] S.H. Koenig, K.E. Kellar, Theory of 1/T1 and 1/T2 NMRD profiles of solutions of magnetic nanoparticles, Magn. Reson. Med. 34 (1995) 227–233, doi:10.1002/mrm.1910340214.

[52] Z. Zhou, L. Yang, J. Gao, X. Chen, Structure–relaxivity relationships of magnetic nanoparticles for magnetic resonance imaging, Adv. Mater. 31 (2019) 1804567, doi:10.1002/adma.201804567.

[53] B.H. Kim, M.J. Hackett, J. Park, T. Hyeon, Synthesis, characterization, and application of ultrasmall nanoparticles, Chem. Mater. 26 (2014) 59–71, doi:10.1021/cm402225z.

[54] J.R. Davis, Handbook of Materials for Medical Devices, ASM International, Ohio, USA, 2003.

[55] T. Furuzono, M. Masuda, M. Okada, S. Yasuda, H. Kadono, R. Tanaka, K. Miyatake, Increase in cell adhesiveness on a poly(ethylene terephthalate) fabric by sintered hydroxyapatite nanocrystal coating in the development of an artificial blood vessel, ASAIO J 52 (2006) 315–320, doi:10.1097/01.mat.0000214860.08820.f9.

[56] S. Anjum, A. Gupta, D. Sharma, S. Kumari, P. Sahariah, J. Bora, S. Bhan, B. Gupta, Antimicrobial nature and healing behavior of plasma functionalized polyester sutures, J. Bioact. Compatible Polym. 32 (2017) 263–279, doi:10.1177/0883911516668665.

[57] S. Huang, J. Liu, D. Liu, Q. Yuan, Facile and large-scale synthesis of Gd(OH)3 nanorods for MR imaging with low toxicity, New J. Chem. 36 (2012) 1335–1338, doi:10.1039/C2NJ21009F.

[58] Q.Z. Yao, S.H. Yu, T.L. Zhao, F.J. Qian, H. Li, G.T. Zhou, S.Q. Fu, Enhanced potential toxic metal removal using a novel hierarchical SiO2-Mg(OH)(2) nanocomposite derived from sepiolite, Minerals 9 (2019) 298, doi:10.3390/min9050298.

[59] L. Wang, Y. Jia, Q. Yu, Y. Wu, Magnetic fiber material and preparation method and application thereof, China Patent. No. ZL202010025304 9 (2021).

[60] C.Z. Chen, L.G. Wang, Y. Huang, Ultrafine electrospun fibers based on stearyl stearate/polyethylene terephthalate composite as form stable phase change materials, Chem. Eng. J. 150 (2009) 269–274, doi:10.1016/j.cej.2009.03.007.

[61] K.P. Matabola, R.M. Moutloali, The influence of electrospinning parameters on the morphology and diameter of poly(vinyledene fluoride) nanofibers-effect of sodium chloride, J. Mater. Sci. 48 (2013) 5475–5482, doi:10.1007/s10853-013-7341-6.

[62] K. Arayanarakul, N. Choktaweesap, D. Aht-ong, C. Meechaisue, P. Supaphol, Effects of poly(ethylene glycol), inorganic salt, sodium dodecyl sulfate, and solvent system on electrospinning of poly(ethylene oxide), Macromol. Mater. Eng. 291 (2006) 581–591, doi:10.1002/mame.200500419.

[63] L. Wang, M. Wang, P.D. Topham, Y. Huang, Fabrication of magnetic drug-loaded polymeric composite nanofibres and their drug release characteristics, RSC Adv 2 (2012) 2433–2438, doi:10.1039/c2ra00484d.

[64] G. Kaur, P. Sharma, R. Priya, O.P. Pandey, Thermal dehydration kinetics involved during the conversion of gadolinium hydroxide to gadolinium oxide, J. Alloys Compd. 822 (2020) 153450, doi:10.1016/j.jallcom.2019.153450.

[65] Z. Zhou, Z. Zhao, Z. Hui, Z. Wang, J. Gao, Interplay between longitudinal and transverse contrasts in Fe3O4 nanoplates with (111) exposed surfaces, ACS Nano 8 (2014) 7976–7985, doi:10.1021/nn5038652.

[66] S. Fakirov, Handbook of Thermoplastic Polyesters: Homopolymers, Copolymers, Blends, and Composites, WILEY-VCH, Weinheim, German, 2002.

[67] S. Kumagai, S. Hirahashi, G. Grause, T. Kameda, H. Toyoda, T. Yoshioka, Alkaline hydrolysis of PVC-coated PET fibers for simultaneous recycling of PET and PVC, J. Mater. Cycles Waste Manage. 20 (2018) 439–449, doi:10.1007/s10163-017-0614-4.

[68] M. Li, T. Deng, S. Liu, F. Zhang, G. Zhang, Superhydrophilic surface modification of fabric via coating with nano-TiO2 by UV and alkaline treatment, Appl. Surf. Sci. 297 (2014) 147–152, doi:10.1016/j.apsusc.2014.01.105.

[69] Z. Zhou, Z.-R. Lu, Gadolinium-based contrast agents for magnetic resonance cancer imaging, WIREs Nanomed. Nanobiotechnol. 5 (2013) 1–18, doi:10.1002/wnan.1198.

[70] M. Marquez, A. Robben, B.P. Grady, I. Robb, Viscosity and yield stress reduction in non-colloidal concentrated suspensions by surface modification with polymers and surfactants and/or nanoparticle addition, J. Colloid Interface Sci. 295 (2006) 374–387, doi:10.1016/j.jcis.2005.10.016.

[71] E.P.S. Tan, S.Y. Ng, C.T. Lim, Tensile testing of a single ultrafine polymeric fiber, Biomaterials 26 (2005) 1453–1456, doi:10.1016/j.biomaterials.2004.05.021.

[72] A. Baji, Y.-W. Mai, S.-C. Wong, Effect of fiber size on structural and tensile properties of electrospun polyvinylidene fluoride fibers, Polym. Eng. Sci. 55 (2015) 1812–1817, doi:10.1002/pen.24020.

[73] M. Rogosnitzky, S. Branch, Gadolinium-based contrast agent toxicity: a review of known and proposed mechanisms, BioMetals 29 (2016) 365–376, doi:10.1007/s10534-016-9931-7.